Self-Assembly of a Ginkgo Oligomerization Domain Creates a Sub-10-nm Honeycomb Architecture on Carbon and Silicon Surfaces with Customizable Pores: Implications for Nanoelectronics, Biosensing, and Biocatalysis

Elise Jacquier, Pierre-Henri Jouneau, Denis Falconet, Denis Mariolle, Emmanuel Thévenon, Grégory Si Larbi, Raluca Tiron, François Parcy, Pierre-Henri Elchinger, Renaud Dumas

Self-Assembly of a Ginkgo Oligomerization Domain Creates a Sub-10-nm Honeycomb Architecture on Carbon and Silicon Surfaces with Customizable Pores: Implications for Nanoelectronics, Biosensing and Biocatalysis

Elise Jacquier, Pierre-Henri Jouneau, Denis Falconet, Denis Mariolle, Emmanuel Thévenon, Grégory Si Larbi, Raluca Tiron, François Parcy*, Pierre-Henri Elchinger*, and Renaud Dumas*

KEYWORDS: helical polymer, tunable pore, nanomaterial, protein nanostructure, nanopatterning, green technology

ABSTRACT.

Over the last decade, protein self-assembly techniques have been extensively studied and improved, enabling the production of a wide range of different nanometric patterns. However, most studies in this field depict thin self-assemblies of a few nanometers in height, while precise grafting of molecules on the patterns remains challenging. We present here a natural polymeric honeycomb organization based on the self-assembly abilities of a *Ginkgo biloba* protein oligomerization domain. This honeycomb architecture depicts 3D pores of 5 nm diameter and a height of 40 stacked proteins. Each protein has tunable N- and C-terminal extensions located inside the pore allowing different binding of ligands in the pore. The proof of concept is illustrated here by the distinctive metallization of the pores with nickel or gold. Overall, these characteristics make this honeycomb a versatile platform paving the way for major biotechnological advances that were not possible with current nanomaterials.

1. Introduction

Nanopatterning of surfaces using biological macromolecules such as DNA, peptides and proteins has become a highly active field of research yielding many technological breakthroughs. Due to their self-assembling ability, biological macromolecules have been widely used as scaffold for the construction of nanomaterials[1–4]. Among these macromolecules, proteins with their 20 different amino acids, offer flexibility in self-assembled structures with nanometric specifications. The initial objective in protein self-assembly was to obtain regular, robust and wide 2D layers with controlled height and organization. Nowadays, these protein lattices are studied to evaluate their usefulness for nanotechnological applications.

Over the years, different types of bottom-up processes have been implemented to generate protein self-assemblies on surfaces (Table S1). Pioneering work began with self-assembly of T-layer[5] and S-layer[6] proteins[7–9] which are still used as biomaterial[9,10]. So far, the creation of self-assembled 2D protein networks for nanotechnological applications has been achieved mainly through the design and engineering of protein interfaces from known 3D crystallographic structures (Table S1), with new interfaces created by different types of interactions such as disulfide bridge[11–15], metal-induced interactions[14–21], hydrophobic interactions[15,22,23], as well as the addition of fused amyloid domains[24]. Complex processes have been also used to tune protein network based on ligand-receptor models [25–27], streptavidin-Streptag affinity[28] or covalent coupling by enzymatic catalysis[29]. Finally, promising de novo approaches have also been used to predict and generate different protein/protein[30,31] and protein/inorganic surface interfaces[32] for tunable protein self-assemblies.

Overall, current studies have shown that self-assembly of proteins on surfaces allows the creation of mesoporous nanomaterials with different pore shapes and sizes. These self-assembled

pores can be used as grafting sites for nanotechnology applications[13,29]. However, most current self-assemblies do not offer the possibility to modulate both type and number of grafting sites which depend on i) the amino acid sequence and ii) the number of protein blocks composing the pore, often limited to a small number (4-6) of monomers.

Here, to overcome this challenge, we propose to use the Sterile Alpha Motif (SAM) domain of the LEAFY (LFY) protein from the *Ginkgo biloba* (GbLFY) tree. In Nature, the LFY protein is a transcription factor, studied for its role in controlling plant meristem division, differentiation, and flower development[33,34]. The SAM domain of GbLFY (GbLFY-SAM) self-assembles to form a helical polymer through head-tail interactions. This polymer interlocks with six others leading to a honeycomb structure with an 8 nm pitch (distance between two neighboring pores) (Fig. 1). Each helical polymer has a 5-nm pore (Fig. 1) in which a disordered and modular C-terminal extension of each monomer is located. In solution, self-assembly leads to exceptionally robust micrometer hexagonal crystals that can be functionalized inside the pore[33,35]. The robustness of the honeycomb relies on the tight interaction between the edge of each helical polymer and the groove of its six neighbors (Fig. 1). Whether this 3D modular honeycomb architecture can occur on surfaces has remained elusive. In this paper, we have successfully formed a honeycomb on different surfaces thank to the addition of a N-terminal extension. Each helical polymer of the honeycomb is built by about 40 stacked functionalizable proteins. Moreover, the pore lumen of each helical polymer can be modified by N- or C-terminal extension modifications without affecting the self-assembly. The concept of specific grafting into the honeycomb pores is illustrated here by differential metallization of the pores with nickel or gold.

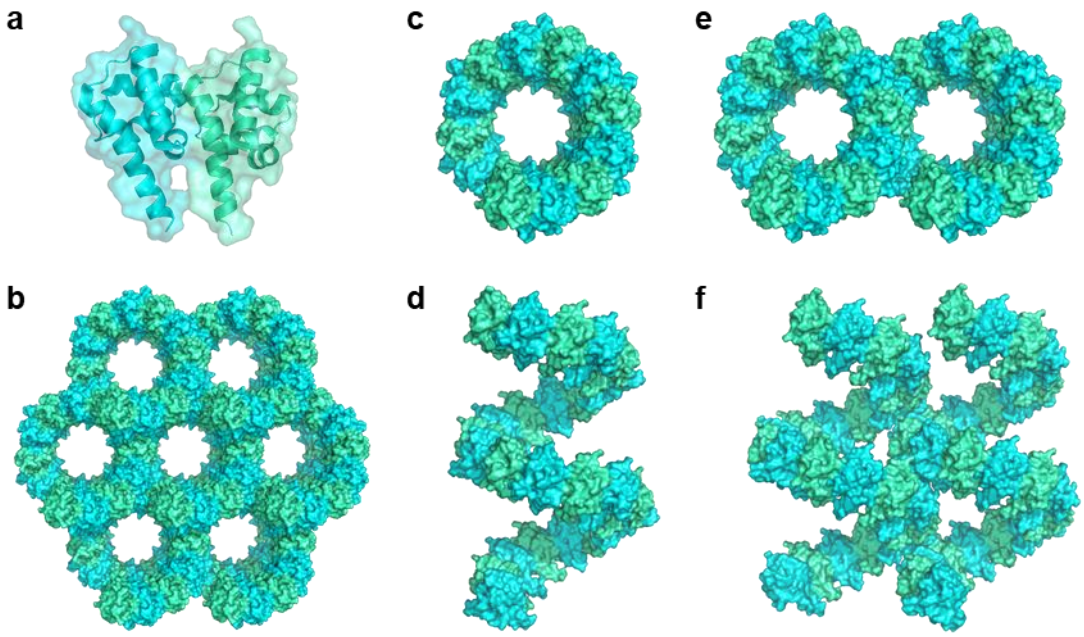

Figure 1. Polymeric honeycomb structure of the SAM oligomerization domain of the GbLFY protein mediated through head tail interactions. (a) GbLFY-SAM asymmetric unit (PDB: 4UDE) showing the interaction of two monomers. (b) Each helical polymer interacts with six neighbors leading to the honeycomb architecture. Each helical polymer has a 5-nm pore and the distance between two neighboring pores is 8 nm. (c) and (d) detail of one helical polymer. (e) and (f) interactions between two helical polymers. In the schemes (b-f), only 22 monomers are shown for each helix (instead of 40 determined by AFM).

2. Methods

2.1 Protein synthesis and purification. GbLFY-SAM is composed of an 87-amino-acid core SAM oligomerization domain surrounded by 24 N- and 23 C-terminal residues. The N-terminal extension contains a 6-histidine tag used for affinity purification and a cleavage site whereas the C-terminal extension contains a disordered sequence. These residues remain invisible by X-ray crystallography (Fig. 1) because of their flexible structure, but their presence was confirmed by mass spectrometry[35]. GbLFY-SAM proteins were expressed in *Escherichia coli* BL21(DE3) strain. First, cells were transformed with pETM11 plasmid coding for a N-terminal histidine-tag and a cleavage site for TEV (referred as N-terminal extension) followed by the sequence corresponding to GbLFY-SAM wild type protein[33]. Transformed cells were used to inoculate 1 L Luria-Bertani (LB) medium supplemented with 1 mL of kanamycin at 50 mg.mL-1 and 1 mL of chloramphenicol at 34 $mg.mL^{-1}$. Cells were grown at 37°C under agitation up to an optical density of 0.6 at 600 nm. Temperature is then shifted to 18°C for 1 hour. IPTG (0.4 mM) is added to the culture and growth continues at 18°C overnight before cells pelleting. Pellets corresponding to 0.25 L culture are sonicated in 50 ml buffer A (20 mM Tris-HCl pH 8.0, 1 mM TCEP) supplemented with one protease inhibitor tablet (ThermoFischer). After centrifugation (45 min at 15 000 g), the supernatant is loaded on a Ni-Sepharose High Performance column pre-equilibrated in buffer A. The column is then washed with buffer A containing 20 mM imidazole and proteins are eluted with buffer A containing 300 mM imidazole. SDS-PAGE was performed to evaluate elution fraction purity. Then, eluted fractions were dialyzed overnight against buffer A and concentrated using Amicon Ultra Centrifugal filters (Merck) until 5 $mg.mL^{-1}$. Proteins were then flash frozen and stored at -80°C.

Cysteine mutant K110C, GGSGGSCHCHCHC mutant and shorter C-terminal extension were obtained by gene synthesis (ShineGene) from the initial GbLFY-SAM sequence cloned in pETM11[33]. For the shorter N-terminal extension mutants, the nucleotide sequence corresponding to seven (MHHHHHH) or the first nine (MKHHHHHHP) amino acids of the pETM11 tag was inserted in the 5' side of the sequence of GbLFY-SAM in a pET-30a (+) plasmid. The main problem with mutants modified on their N-terminal or C-terminal extension is that their ability to oligomerize via head-tail interactions has been increased, leading to the aggregation of large oligomers. To solve this problem during purifications, mutated proteins are purified in buffers containing 40-200 mM CAPS-NaOH pH 10.5 in the presence of 50-500 mM NaCl and 1 mM TCEP. The proteins are then dialyzed in a 40 mM CAPS-NaOH pH 10.5 buffer containing 50 mM NaCl and 1 mM TCEP before being used to form self-assemblies. Shorter protein without His-tag was obtained by cleavage overnight with the TEV protease (5% w/w) and the cleaved protein was purified on a Ni-Sepharose High Performance column[33]. Amino acid sequence of the different proteins used in this work are described in the Table S2.

2.2 Self-assembly onto TEM grids. To perform protein self-assembly, vapor diffusion sitting drop method was used. A 18 µL drop composed by GbLFY-SAM solution and crystallization buffer is deposed in a well chamber while the reservoir chamber contains only buffer crystallization. Optimum conditions were obtained by mixing 6 µL of a 2.5 $mg.mL^{-1}$ GbLFY-SAM solution with 12 µL of the reservoir solution containing 20 mM Tris HCl pH 8.0, 1 mM TCEP and 315 mM ammonium sulfate. A 200 mesh gold TEM grid coated with a pure carbon film (TED Pella) or SiO_2 grid (SIMPore) was hydrophilized using a plasma glow discharge (Cordouan Technologies) at 2 mA for 40 seconds under 2.10^{-1} mbar and then put on the top of the drop. For

the experiments with SiN grid (TED Pella) either hydrophilic (coated with hydroylated alumina) or hydrophobic (coated with alumina and fluoro-methyl-silane), no glow discharge was performed. After closing of the crystallization chamber, self-assemblies were allowed to grow at 20°C for 24 h. The same protocol was used for experiments with shorter N- or C-terminal extension.

2.3 Negative staining for STEM experiments. After 24h crystallization, the grid is incubated with a 18 µL drop of 2% uranyl acetate for 2 minutes. Liquid excess was then removed by capillarity with a filter paper and grid was air-dried. Self-assemblies were imaged with STEM mode using a Zeiss Merlin microscope. Images were collected using both bright field and dark field detectors at 30 kV with a beam current of 240 pA with magnification between 2 KX and 135 KX.

2.4 Metallization and chemical analysis of the self-assembly. After 24h crystallization, the grid is incubated with a 18 µL drop of Ni^{2+} salt (Hampton Research) or gold salt (Sigma-Aldrich). For nickel salt ($NiCl_2$), a range of concentration from 0.18 mM (*i.e.* 10 equivalents relative to protein amount) to 1.79 mM (*i.e.* 100 equivalents relative to protein amount) was tested. In the same way, a range from 0.23 mM (*i.e.* 10 equivalents relative to protein amount) to 2.30 mM (*i.e.* 100 equivalents relative to protein amount) of gold salt ($HAuCl_4$) has been investigated. Moreover, time incubation from 2 to 10 min has been considered. The optimal conditions are 0.53 mM (*i.e.* 30 equivalents relative to protein amount) for nickel salt and 0.23 mM for gold salt with an incubation time of 5 min in both cases. Then, for reduction step, a 18 µL drop of $NaBH_4$ at a final concentration of 32 mM was made and the grid was put on top of this drop allowing reduction to occur for 5 min. Liquid excess was then removed by capillarity with a filter paper and grid was

air-dried. STEM images were collected in the same microscope than the negative staining experiments at 30 kV but using only dark field detector. EDX spectrum of the metallized sample was acquired on a FEI Osiris microscope operated at 200 kV using a Super X Detector (Bruker).

2.5 AFM imaging. For AFM experiments, self-assemblies were imaged directly on the TEM grid or silicon wafer using PeakForce Tapping mode in air with ScanAsyst Air probes (Bruker) on a Dimension XR AFM (Bruker). The ScanAsyst Air probes used in all the experiments have a spring constant of 0.25 N/m. Images were collected with a resolution of 1024 lines and a scan rate between 0.5 and 0.2 Hz. Scan analysis was performed using Gwyddion software (http://gwyddion.net). Scans were base flattened and zero was fixed before height measurements using the profile tool. Then, an adjusting function is fitting on each self-assembly profile to extract its height. Average height (Hn) was determined by measuring individual heights (Hi) of at least 30 self-assemblies (ni) such as (1). Standard deviation (σn) is determined by (2).

$$H_n = \frac{\sum_{i=1}^{n} n_i H_i}{\sum_{i=1}^{n} n_i} \quad (1)$$

$$\sigma_n = \sqrt{\frac{\sum_{i=1}^{n} (H_i - H_n)^2}{n}} \quad (2)$$

2.6 Image analyses. Thanks to Fiji software (http://imagej.net/Fiji), STEM image contrast was enhanced by removing the background through background subtraction. Surface analysis was performed by applying a threshold on the image, then particle analysis was performed to determine the overall coverage of the self-assemblies. To detect the self-assembly pores, a threshold and a Mexican Hat Filter were used to reduce noise in the images. The number of pores detected was counted by finding the maximal edges on the image. Lattice parameters of the self-assemblies were

measured using the Fast Fourier Transform calculation. This analysis yields the power spectrum of the STEM images, whereby each frequency is associated to angle and radii related to the lattice parameters of the self-assemblies.

3. Results and Discussion

3.1 Orientation of the honeycomb on a carbon surface. GbLFY-SAM honeycomb oligomerization has been previously observed to form 3D crystals[33]. It is a head-tail interaction involving mainly ionic and hydrogen bonds, as determined using mutations affecting either the head or the tail side[33]. Based on the same crystallographic method, we aimed to reproduce the GbLFY-SAM honeycomb self-assembly on a surface. We opted for a carbon grid surface that facilitates the characterization of protein assemblies by scanning transmission electron microscopy (STEM) after negative staining. During the first attempts, the cleaved GbLFY-SAM domain[33] , devoid of its N-terminal extension, formed supramolecular helices lying parallel to the surface grid without forming an apparent honeycomb (Fig. 2 and Fig. S1).

To determine whether the N-terminal extension initially present on the protein could have a role in the orientation of the self-assembly, we repeated the experiments with the uncleaved protein. STEM images of the self-assembly of GbLFY-SAM with its N-terminal extension revealed black dots corresponding to the pores of the honeycomb oriented perpendicular to the carbon grid (Fig. 2, Fig. 3 and Fig. S1). To further check whether residual Ni^{2+} from the Ni-NTA column was not responsible for the self-assembly by promoting interaction between the N-terminal extensions (e.g. the histidine tag), we performed the same experiment in the presence of EDTA, a Ni^{2+} chelator. The STEM images (Fig. S2) showed that the honeycomb architecture was not affected by EDTA supporting the absence of Nickel effect on the self-assembly.

Since the N-terminal extension was not present in the X-ray structure of the 3D crystals growing in solution [33] we used the I-TASSER modelling server[36] to elucidate its position (Fig. S3). Based on this model, the N-terminal extension of each monomer is not found in the same pore as the C-

terminal extension but in an adjacent pore (Fig. S3). However, in the honeycomb, both N- and C-terminal extensions are located within the pores (Fig. S3).

Next, we determined which part of the 23 amino acids of the N-terminal extension was key for perpendicular honeycomb orientation. By successively deleting the amino acids of the N-terminal extension starting from the ones closest to GbLFY-SAM core, we established that the first six histidine residues are sufficient for this orientation (Fig. 3 and Fig. S4). The presence of the N-terminal extension likely allows interaction with the grid and perpendicular growth of the honeycomb. Alternatively, the absence of the N-terminal extension could induce a large formation of 3D crystals in solution, depleting the protein available for surface crystallization.

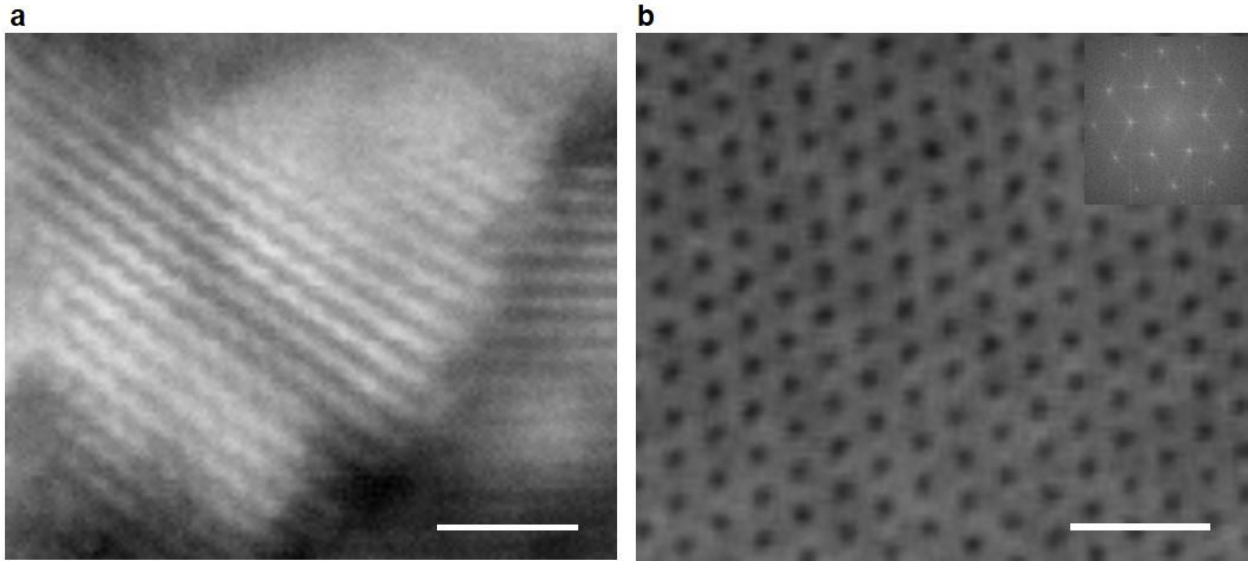

Figure 2. Orientation of the GbLFY-SAM honeycomb depends on the N-terminal extension. (a) Self-assembly of GbLFY-SAM domain without N-terminal extension. (b) Self-assembly of GbLFY-SAM domain with a N-terminal extension. Each black dot corresponds to a pore of the self-assembly. The Fast Fourier Transform shown in inset indicates that GbLFY-SAM with the N-terminal extension forms an architecture (8 nm pitch and 5 nm lumen diameter) similar to the ones measured in the X-Ray crystal structure of the GbLFY-SAM crystallized in solution[33] without the N-terminal extension. The self-assembly on surfaces uses the same mechanism as 3D crystals. A double mutant (one mutation in the head face and another one in the tail face) is not able to create the honeycomb structure. The scale bars are 30 nm on both images.

3.2 Characterization of the honeycomb growth on carbon and silicon surfaces. Self-assembly of molecules onto surfaces often lead to miss folding or defect in the lattice[37]. Here, Fast Fourier Transform (FFT) calculations, performed on STEM images of the GbLFY-SAM honeycomb array, reveals lattice parameters (a = b = 8.2 (+/- 0.1) nm et γ = 120 (+/- 1) °) identical to those found on the crystal by X-ray diffraction[33] (Fig. 2 and 3, Fig S1, S2 and S4).

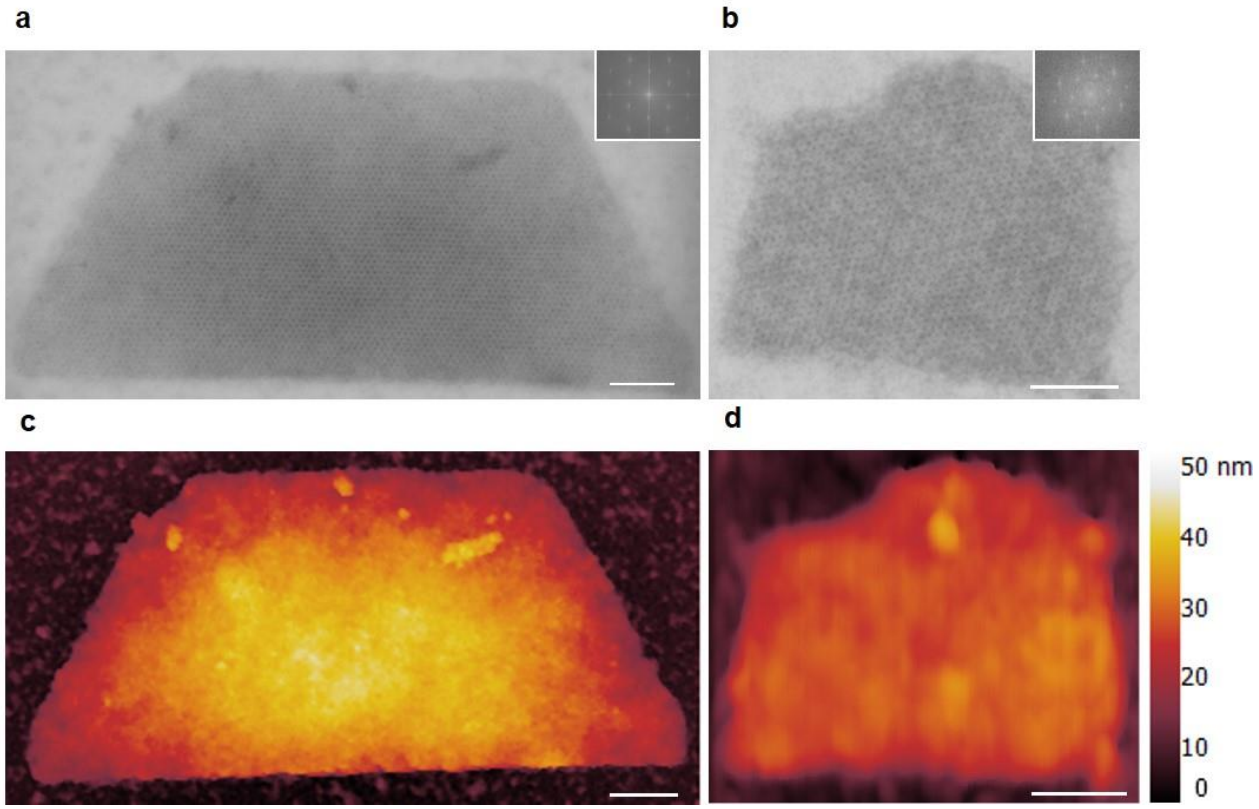

Figure 3. The N-terminal extension of GbLFY-SAM can be reduced to 6 Histidine residues. (a) STEM image of the GbLFY-SAM with N-terminal extension. (b) STEM image of the GbLFY-SAM with a N-terminal extension corresponding to the first 9 amino acids containing the first six histidine residues. Similar organization was obtained with a shorter N-terminal extension containing only the N-terminal methionine and six histidine residues. (c) Height of the self-assembly shown in (a) using AFM. (d) Height of the self-assembly shown in (b) measured using AFM. Fourier transform calculation show that the GbLFY-SAM with its N-terminal extension and the mutant with a shorter N-terminal extension disclose similar lattice parameters. AFM measurements indicate that both self-assemblies have an average height of 31 nm. The scale bars are 200 nm for all four images.

In solution, the head-tail interactions extend to several monomers to create an helical oligomers of a limited sized of about 8 monomers at a protein concentration of 4.5 mg/ml as demonstrated by SEC-MALLS experiments[33]. Under crystallization conditions, the helices can grow to larger sizes and each helix interacts with six other helices to form a honeycomb structure[33]. The 3D crystals can reach 500 µm in length and 50 µm in width. However, the self-assemblies grown on carbon grid are thinner. Correlative microscopy between STEM and Atomic Force Microscopy (AFM) was performed and the AFM (Fig. 3) measurements indicated a height of 31 (+/- 5) nm, corresponding to a stacking of around 40 oligomerization domains (Fig. 3 and Fig. S5). We also determined that the height of the shorter N-terminal mutant is similar to GbLFY-SAM (Fig. 3). Overall, the protein honeycomb covers around 10 % of the grid, with individual crystals of up to 0.3 μm^2.

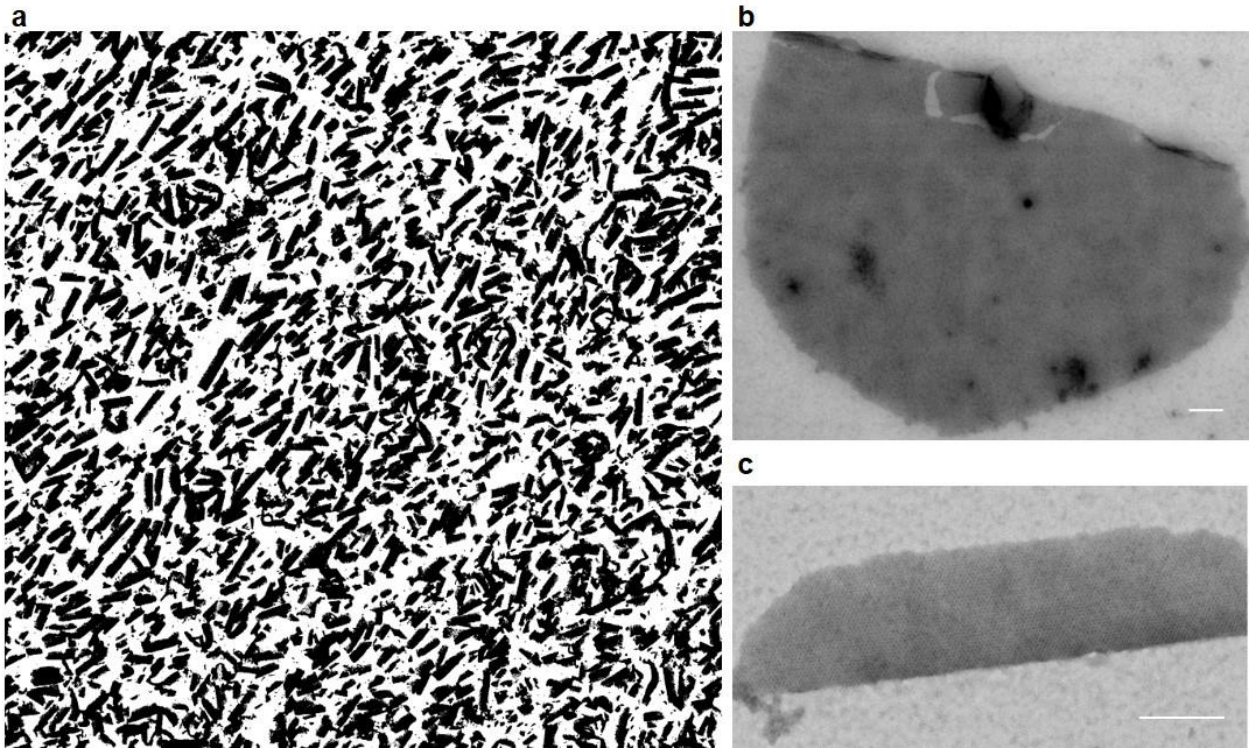

Figure 4. Surfaces covered by GbLFY-SAM with its N-terminal extension after carbon grid treatment using glow discharge. (a) The use of a threshold in ImageJ to detect self-assemblies on STEM images reveals a cover up to 54 % of the carbon surface. This image is a 20 x 20 μm^2 area.

(b), (c) The surface of individual self-assemblies varies from 0.3 μm^2 (c) to 4.9 μm^2 (b). The scale bars are 200 nm on all the images.

For nanotechnological applications, large scale nanopatterning is required[38]. Moreover, amorphous carbon used to coat the EM grid is not a suitable substrate for these applications as it does not conduct electrons. In order to overcome these limitations, we adjusted our protocol. First, we attempted to increase the surface covered by the self-assembly, by glow discharging the grids to hydrophilized them. The total area covered by the honeycomb increased by up to 54%, with individual self-assembly surface up to 4.9 μm^2 (Fig. 4). These observations suggest that the honeycomb binds on the grid surfaces through weak polar interactions. Whatever the protein concentration (0.625 to 2.5 $mg.mL^{-1}$), a mixture of shapes is obtained of which the trapezium (Fig. 3a) and its elongated form (Fig. 4c) in one dimension are the most representative.

Then, we changed the carbon substrate to silicon wafers widely used in nanoelectronic applications. We succeeded in reproducing such assemblies on silicon grids and wafers and obtained a similar honeycomb architecture as revealed by STEM (Fig. 5a). It is noteworthy that the change in the surface (silicon wafer or carbon grid) does not affect the height of the GbLFY-SAM lattice (Fig. 5b) neither the lattice parameters. To further investigate the influence of the surface properties on the self-assembly, we also tried hydrophilic and hydrophobic commercial silicon nitride grid (Fig. S6). These grids are coated respectively with hydroxylated alumina and alumina plus fluoro-methyl-silane. There is no difference between the hydrophilic and the hydrophobic coating on the GbLFY-SAM self-assembly. In addition, the lattice parameters are also the same as the ones on carbon and silicon surface. Altogether, these results show that self-assembly can take place on a wide variety on surfaces.

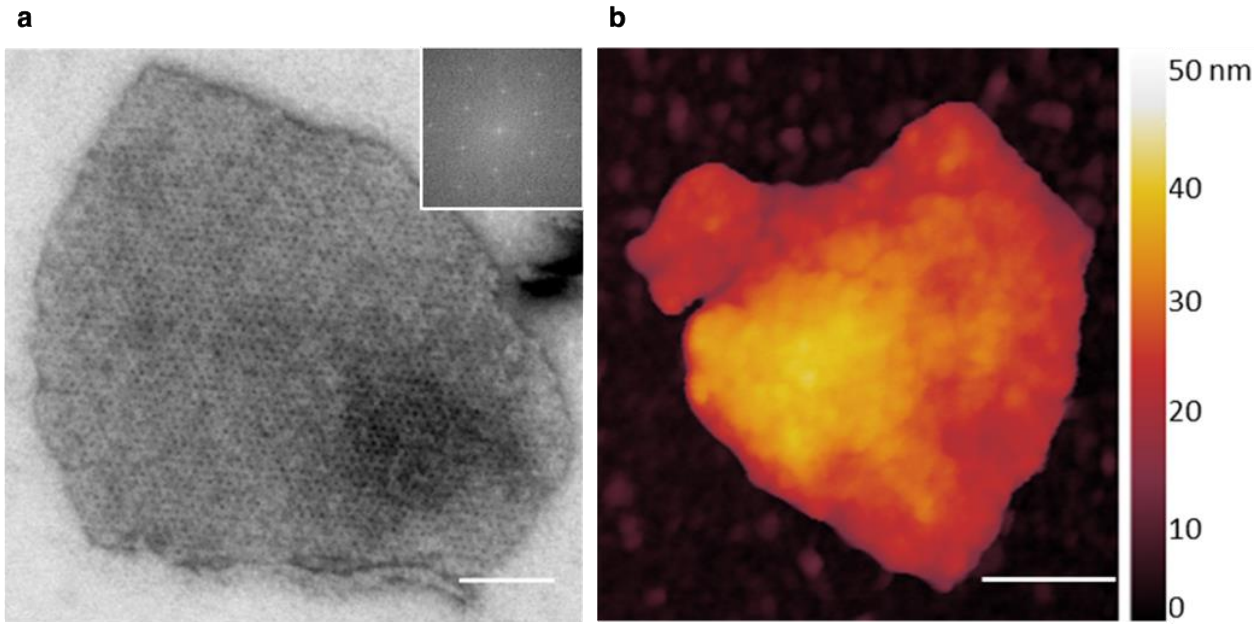

Figure 5. Self-assembly of GbLFY-SAM with its N-terminal extension on silicon surface. (a) STEM image of the self-assembly on a silicon grid. Fourier transform image shown in inset indicates dimensions similar to those observed on carbon surface. (b) Height of a GbLFY-SAM self-assembly on a silicon wafer measured using AFM. The scale bars are 100 nm on both images.

3.3 Polymeric honeycomb structure metallization. Finally, one of the key points for the use of the protein self-assemblies in the field of nanotechnology is the functionalization of the pores. To this end, we investigated whether it was possible to selectively metallize the polymeric honeycomb structure. As the N-terminal extension is composed of at least 6 histidine and is facing inside the lattice pores, we aimed at using the specific affinity of histidine for Ni^{2+} to metallize the pores of the self-assembly (Fig. S3). After the crystallization of the GbLFY-SAM self-assembly on the TEM grid, Ni^{2+} salt was added onto the self-assembly for 5 min. Then, $NaBH_4$ was used to reduce Ni^{2+} salt. It is noteworthy that in this experiment, nickel was the only element allowing the staining of the self-assembly in STEM. As expected, metallization of the GbLFY-SAM honeycomb with Ni^{2+} salt reduced occurs inside the pores demonstrating that the N-terminal

extension of GbLFY-SAM is inside the lattice pores (Fig. 6a) as previously modeled. To fully characterize the metallized honeycomb, we also acquired an Electron Dispersive X-ray Spectroscopy spectrum of the self-assembly corroborating the presence of nickel (Fig. 6a). Thus, despite the reduction of Nickel by $NaBH_4$, the honeycomb structure remains intact and FFT calculations of the STEM images showed lattice parameters similar to those measured in STEM images of negative stained GbLFY-SAM self-assembly. Then, we did these experiments in presence of 1 mM EDTA before the salt reduction to check the specific effect of Ni^{2+}. We showed that the chelation of Ni^{2+} by EDTA can block the metallization of the self-assembly which appears unstained in STEM with no characteristic nickel X-ray in the related EDX spectrum (Fig. S7). From these results, it appears that a specific metallization of the pores of the honeycomb lattice is achievable using the advantageous affinity of a metal for amino acid located inside the pores.

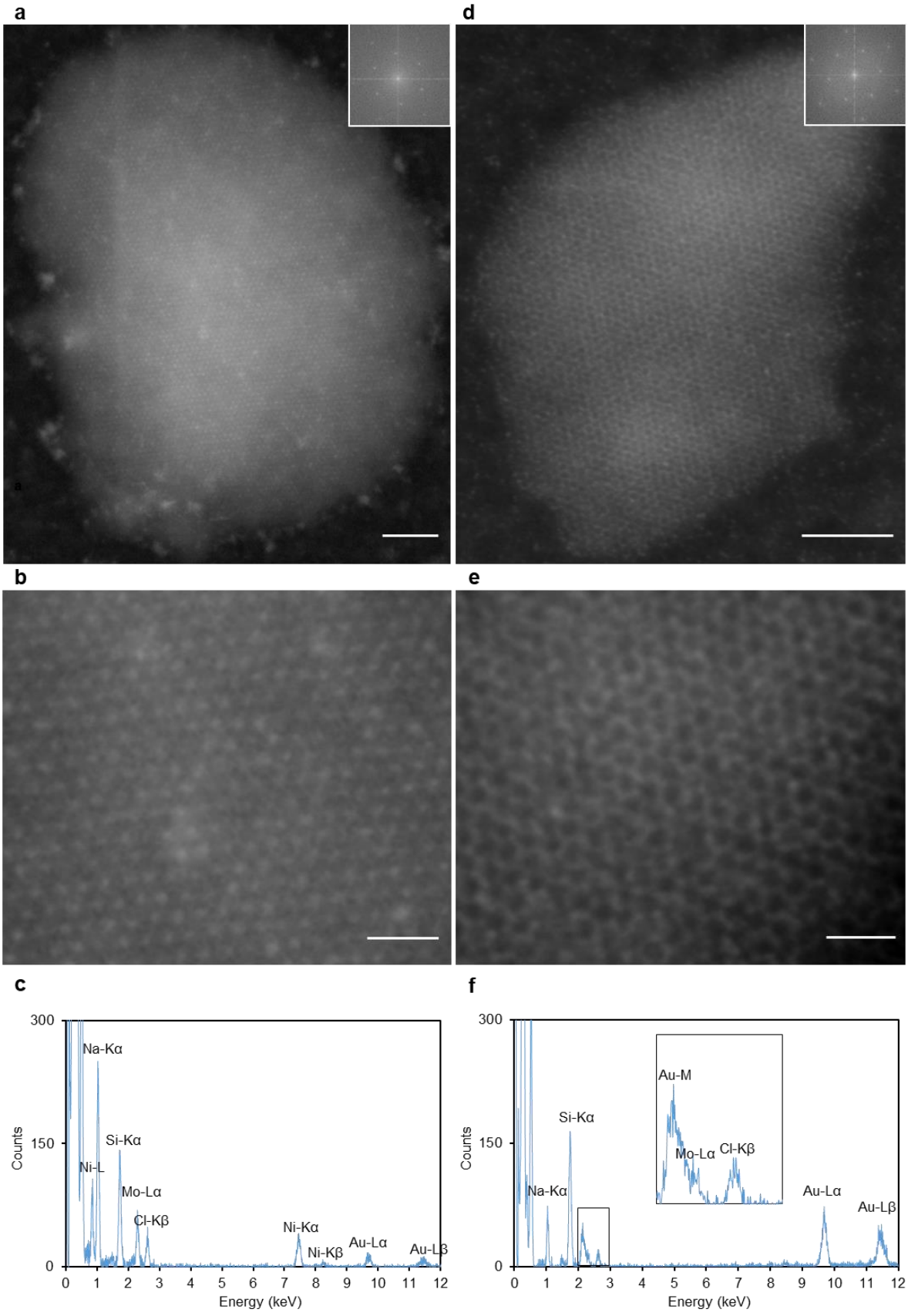
a
d
b
e
c
f
Counts
Energy (keV)
Na-Kα
Si-Kα
Ni-L
Mo-Lα
Cl-Kβ
Ni-Kα
Ni-Kβ
Au-Lα
Au-Lβ
Au-M

Figure 6. Specific metallization of the self-assembly with Ni^{2+} salt (a-c) or Au^{3+} salt (d-f). In these images, the contrast is only provided by the reduced metal. (a) STEM image in dark field mode of a self-assembly with Ni^{2+} salt reduced by $NaBH_4$ inside the pore. (b) Zoom of the STEM image. Scale bar: 30 nm. (c) EDX spectrum of the self-assembly emphasizing the presence of nickel. (d) STEM image in dark field mode of a self-assembly with Au^{3+} salt reduced by $NaBH_4$ outside of the pore. (e) Zoom of the STEM image. Scale bar: 30 nm. (f) EDX spectrum of the self-assembly emphasizing the presence of gold. The inset show a zoom of the pics from 2 to 3 keV to illustrate the overlapping between Au-M and the Mo-Lα. The scale bars are 100 nm on both images.

To further investigate this point, we metallized the honeycomb structure with another metal showing different binding properties. Affinity of gold salt for amino acid have been studied previously[39] showing rather broader interactions and different affinities than Ni^{2+} for histidine.

As expected, the *in situ* reduction of gold salt in the self-assembly does not lead to a specific staining of the inner part of the pores but to the coloration of their outlines (Fig. 6b). This labeling is explained by a higher number of amino acids able to interact with gold in the core oligomerization domain compared to the N- and C-terminal extensions. As in the nickel experiments, gold was the only element allowing the staining of the self-assembly in STEM. Presence of gold on the self-assembly was confirm by acquiring an EDX spectrum (Fig. 6b). These results demonstrated that the honeycomb structure can be metallized either inside or outside of the pore depending on the specific affinity of the amino acid present in the pore for metal salt.

3.4 Honeycomb lattice engineering for futures nanotechnological applications. Metallization of the GbLFY-SAM can be specifically driven inside the honeycomb pores thanks to the affinity of the N-terminal extension histidines for a metal such as Ni^{2+}. Besides, it has been shown that the C-terminal extension of GbLFY-SAM is also facing inside the pore[35]. We investigated if it was possible to modify the amino acids of the C-terminal extension without affecting the oligomerization capacity of the monomer and the honeycomb structure. We aimed to

explore a modification of GbLFY-SAM involving a complete deletion of its C-terminal extension. This modification had an impact on the solubility and stability of the GbLFY-SAM in solution. The deletion of the C-terminal extension makes GbLFY-SAM oligomerization faster and leads to protein precipitation in the classic purification protocol. Nevertheless, after optimization of the purification and surface crystallization protocols, we obtained honeycomb self-assemblies identical to GbLFY-SAM (Fig. S4b).

We also made others C- terminal constructions to emphasize the versatility of the GbLFY-SAM self-assembly. In a first construction, we mutated a lysine into a cysteine residue (GbLFY-SAM K110C) (Fig. S4c) in order to insert a unique cysteine residue for specific grafting. In a second construction, we deleted all the C- terminal part and replace it by the amino acid sequence GGSGGSCHCHCHC (Fig. S4d) containing a linker and three histidine and cysteine residues for specific grafting. For these two mutants, the modification has no impact either on the honeycomb formation or on the lattice parameters.

Thus, both the N- and C-terminal extension of GbLFY-SAM can be modified without affecting the honeycomb self-assembly ability. Engineering these extensions by inserting amino acid residues or sequences capable of reacting with specific organic, inorganic or metallic compounds would make this honeycomb architecture a modular grafting platform. Moreover, this platform could accommodate a large number of grafting sites. Indeed, a surface of 1 μm^2 allows to obtain approximately 12 000 pores. Having determined an average pore height per AFM of 31 nm corresponding to a stacking of 40 monomers, we can estimate a capacity of at least 480 000 specific grafting sites per μm^2 (based on one grafting per monomer) (Fig. S8). Selective grafting on the protein can be easily obtained and many amino acid residues can be used[40,41] as demonstrated with the grafting of a ruthenium-based complex onto modified residues of the pores of 3D-GbLFY-

SAM crystals in solution[35]. The pores of the honeycomb could hold specific grafting of catalysts and chromophores at different positions. Hence, the GbLFY-SAM self-assembly on surface could be easily used as a biocatalysis platform.

In addition, great efforts have been made to produce nanostructures with a sub 10 nm-pitch for microelectronics applications[42]. Indeed, the production of masks for lithography below 10 nm remains difficult and expensive[43,44]. Among all the lithographic techniques, block copolymers remain one of the main technologies currently studied to overcome this challenge[45]. The use of the GbLFY-SAM honeycomb as a hard mask (Fig. S8) represents a promising opportunity that could compete with the technology of block copolymers[46,47]. Combining photo-etching or chemical etching (*e.g.* hydrofluoric acid) with a modified GbLFY-SAM with short N- and C-terminal extension making the honeycomb pore emptier could lead to an etching of sub 10 nm-pitch motif.

Nanoelectronics is not the only field in which the 5 nm modifiable pores of GbLFY-SAM could be useful. Honeycomb pores could also be exploited to build nanopillars by grafting and stacking metallic nanoparticles or quantum dots for use in photovoltaic devices[48,49]. In addition, the graftable pores of GbLFY-SAM, which are almost 10 times smaller in diameter than those currently being tested, could offer an interesting opportunity to increase photovoltaic yield[50]. Closely and evenly spaced metallic nanopillars would also create a dense network that could also improve the signal of biosensor devices for the detection of lower molecular concentrations[51–53]. Whether these 8-nm pitch arrays of 5 nm nanopillars increase efficiency or provide new properties – due specifically to quantum effects – is an open question.

4. Conclusion

In summary, we present here the natural self-assembly capabilities of a *Ginkgo biloba* protein oligomerization domain, building a robust honeycomb architecture with a pitch of 8 nm and 3D pores of 5 nm diameter. Our results show that the orientation of this honeycomb can be controlled on different surfaces. Furthermore, we have shown that the N- and C-terminal extensions can be modified without altering the self-assembly and that the amino acids present on these extensions can be used to specifically metallize the inside or the outside of the pores. Engineering the extensions of the oligomerization domain by inserting amino acid sequences capable of reacting with specific organic, inorganic or metallic compounds will make this honeycomb architecture a modular grafting platform for an extensive range of applications covering biocatalysis, biosensing, or photovoltaic. Moreover, the pores formed by 40 stacked oligomerization domains lead to a huge number of grafting sites above 500 000 per μm^2. In addition to the specific grafting possibilities, the nanometric dimensions of the honeycomb architecture are a promising opportunity to produce masks for lithography processes that could compete with current technologies such as block copolymers.

In conclusion, the possibility of modifying the pore composition for etching or specifically grafting a large number of molecules makes this Ginkgo self-assembled honeycomb a new and unique green nanomaterial pioneering major biotechnological breakthroughs previously impossible with current nanomaterials.

ASSOCIATED CONTENT

Supporting Information

Overview on protein self-assembly, amino acid sequence of N- and C-terminal extensions, superposition of GbLFY-SAM crystallographic structure on STEM image, STEM image with

EDTA, localization of the N- and C-terminal extension in the honeycomb, STEM images of engineered N- and C-terminal, AFM scan of multiple honeycomb, STEM images on hydrophilic and hydrophobic surfaces, desorption of Nickel salt with EDTA, self-assembly as a platform for specific grafting of a huge number of ligands.

AUTHOR INFORMATION

Corresponding Authors

Renaud Dumas - Univ. Grenoble Alpes, CNRS, CEA, INRAE, IRIG-DBSCI-LPCV, 38000 Grenoble, France. Email: renaud.dumas@cea.fr

Pierre-Henri Elchinger - Univ. Grenoble Alpes, CEA, CNRS, IRIG-DIESE-SYMMES, 38000 Grenoble, France. Email: pierre-henri.elchinger@cea.fr

François Parcy - Univ. Grenoble Alpes, CNRS, CEA, INRAE, IRIG-DBSCI-LPCV, 38000 Grenoble, France. Email: francois.parcy@cea.fr

Authors

Elise Jacquier - Univ. Grenoble Alpes, CNRS, CEA, INRAE, IRIG-DBSCI-LPCV, 38000 Grenoble, France. Univ. Grenoble Alpes, CEA, CNRS, IRIG-DIESE-SYMMES, 38000 Grenoble, France.

Pierre-Henri Jouneau - Univ. Grenoble Alpes, CEA, CNRS, IRIG-DIESE-MEM, 38000 Grenoble, France.

Denis Falconet - Univ. Grenoble Alpes, CNRS, CEA, INRAE, IRIG-DBSCI-LPCV, 38000 Grenoble, France.

Denis Mariolle - Univ. Grenoble Alpes, CEA, LETI, MINATEC Campus, 38000 Grenoble, France.

Emmanuel Thévenon - Univ. Grenoble Alpes, CNRS, CEA, INRAE, IRIG-DBSCI-LPCV, 38000 Grenoble, France.

Grégory Si Larbi - Univ. Grenoble Alpes, CNRS, CEA, INRAE, IRIG-DBSCI-LPCV, 38000 Grenoble, France.

Raluca Tiron - Univ. Grenoble Alpes, CEA, LETI, MINATEC Campus, 38000 Grenoble, France.

Author Contributions

E.J., R.T., F.P., P.H.E. and R.D. designed the experiments. E.J., P.H.J., D.F., D.M., E.T., G.S., P.H.E. and R.D. performed the experiments. All authors interpreted the results. E.J., P.H.E. and R.D. wrote the paper with the help of F.P., and input from all authors.

Funding Sources

This work was supported by a CEA program Nanoprot 3D to F.P. and R.T. with a post-doctoral fellowship to P.H.E., a PhD fellowship from the CEA [E.J.], a DRF impulsion grant [to Olivier Hamelin, P.H.E and R.D.], the LabEx Grenoble Alliance for Cell and Structural Biology [ANR-10-LABX-0049 to F.P. and R.D.] and the LabEx Arcane and CBH-EUR-GS [ANR-17-EURE-0003 to P.H.E].

ACKNOWLEDGMENT

We thank Lucile Chiari, Olivier Hamelin, Jean-Luc Putaux, the Nanoprot 3D and A3DN work group (Didier Gasparutto, Xavier Baillin, Robert Baptiste, Caroline Fontenoye, Guillaume Nonglaton, Pascal Mailley), Patrice Rannou and Luc Federzoni for helpful discussions.

REFERENCES

(1) Thiruvengadathan, R.; Korampally, V.; Ghosh, A.; Chanda, N.; Gangopadhyay, K.; Gangopadhyay, S. Nanomaterial Processing Using Self-Assembly-Bottom-up Chemical and Biological Approaches. *Rep. Prog. Phys.* **2013**, *76* (6), 066501. https://doi.org/10.1088/0034-4885/76/6/066501.

(2) Sun, H.; Luo, Q.; Hou, C.; Liu, J. Nanostructures Based on Protein Self-Assembly: From Hierarchical Construction to Bioinspired Materials. *Nano Today* **2017**, *14*, 16–41. https://doi.org/10.1016/j.nantod.2017.04.006.

(3) Fan, S.; Wang, D.; Kenaan, A.; Cheng, J.; Cui, D.; Song, J. Create Nanoscale Patterns with DNA Origami. *Small* **2019**, *15* (26), 1805554. https://doi.org/10.1002/smll.201805554.

(4) Liu, R.; Hudalla, G. A. Using Self-Assembling Peptides to Integrate Biomolecules into Functional Supramolecular Biomaterials. *Molecules* **2019**, *24* (8), 1450. https://doi.org/10.3390/molecules24081450.

(5) Aebi, U.; Smith, P. R.; Dubochet, J.; Henry, C.; Kellenberger, E. A Study of the Structure of the T-Layer of Bacillus Brevis. *J. Supramol. Struct.* **1973**, *1* (6), 498–522. https://doi.org/10.1002/jss.400010606.

(6) Sleytr, U. B. Regular Arrays of Macromolecules on Bacterial Cell Walls: Structure, Chemistry, Assembly, and Function. In *International Review of Cytology*; Elsevier, 1978; Vol. 53, pp 1–64. https://doi.org/10.1016/S0074-7696(08)62240-8.

(7) Gyorvary, E. S.; Stein, O.; Pum, D.; Sleytr, U. B. Self-Assembly and Recrystallization of Bacterial S-Layer Proteins at Silicon Supports Imaged in Real Time by Atomic Force Microscopy. *J. Microsc.* **2003**, *212* (3), 300–306. https://doi.org/10.1111/j.1365-2818.2003.01270.x.

(8) Moll, D.; Huber, C.; Schlegel, B.; Pum, D.; Sleytr, U. B.; Sara, M. S-Layer-Streptavidin Fusion Proteins as Template for Nanopatterned Molecular Arrays. *Proc. Natl. Acad. Sci.* **2002**, *99* (23), 14646–14651. https://doi.org/10.1073/pnas.232299399.

(9) Baneyx, F.; Matthaei, J. F. Self-Assembled Two-Dimensional Protein Arrays in Bionanotechnology: From S-Layers to Designed Lattices. *Curr. Opin. Biotechnol.* **2014**, *28*, 39–45. https://doi.org/10.1016/j.copbio.2013.11.001.

(10) Charrier, M.; Li, D.; Mann, V. R.; Yun, L.; Jani, S.; Rad, B.; Cohen, B. E.; Ashby, P. D.; Ryan, K. R.; Ajo-Franklin, C. M. Engineering the S-Layer of *Caulobacter Crescentus* as a Foundation for Stable, High-Density, 2D Living Materials. *ACS Synth. Biol.* **2019**, *8* (1), 181–190. https://doi.org/10.1021/acssynbio.8b00448.

(11) Zhou, K.; Chen, H.; Zhang, S.; Wang, Y.; Zhao, G. Disulfide-Mediated Reversible Two-Dimensional Self-Assembly of Protein Nanocages. *Chem. Commun.* **2019**, *55* (52), 7510–7513. https://doi.org/10.1039/C9CC03085A.

(12) Nguyen, T. K.; Negishi, H.; Abe, S.; Ueno, T. Construction of Supramolecular Nanotubes from Protein Crystals. *Chem. Sci.* **2019**, *10* (4), 1046–1051. https://doi.org/10.1039/C8SC04167A.

(13) Du, M.; Zhou, K.; Wang, X.; Zhang, J.; Zhang, Y.; Dong, J.; Wu, L.; Qiao, Z.; Chen, G.; Wang, Q. Precise Fabrication of De Novo Nanoparticle Lattices on Dynamic 2D Protein Crystalline Lattices. *Nano Lett.* **2020**, *20* (2), 1154–1160. https://doi.org/10.1021/acs.nanolett.9b04574.

(14) Zhang, J.; Wang, X.; Zhou, K.; Chen, G.; Wang, Q. Self-Assembly of Protein Crystals with Different Crystal Structures Using Tobacco Mosaic Virus Coat Protein as a Building Block. *ACS Nano* **2018**, *12* (2), 1673–1679. https://doi.org/10.1021/acsnano.7b08316.

(15) Suzuki, Y.; Cardone, G.; Restrepo, D.; Zavattieri, P. D.; Baker, T. S.; Tezcan, F. A. Self-Assembly of Coherently Dynamic, Auxetic, Two-Dimensional Protein Crystals. *Nature* **2016**, *533* (7603), 369–373. https://doi.org/10.1038/nature17633.

(16) Heyman, A.; Medalsy, I.; Dgany, O.; Porath, D.; Markovich, G.; Shoseyov, O. Float and Compress: Honeycomb-like Array of a Highly Stable Protein Scaffold. *Langmuir* **2009**, *25* (9), 5226–5229. https://doi.org/10.1021/la804132z.
(17) Brodin, J. D.; Ambroggio, X. I.; Tang, C.; Parent, K. N.; Baker, T. S.; Tezcan, F. A. Metal-Directed, Chemically Tunable Assembly of One-, Two- and Three-Dimensional Crystalline Protein Arrays. *Nat. Chem.* **2012**, *4* (5), 375–382. https://doi.org/10.1038/nchem.1290.
(18) Brodin, J. D.; Carr, J. R.; Sontz, P. A.; Tezcan, F. A. Exceptionally Stable, Redox-Active Supramolecular Protein Assemblies with Emergent Properties. *Proc. Natl. Acad. Sci.* **2014**, *111* (8), 2897–2902. https://doi.org/10.1073/pnas.1319866111.
(19) Zhang, W.; Luo, Q.; Miao, L.; Hou, C.; Bai, Y.; Dong, Z.; Xu, J.; Liu, J. Self-Assembly of Glutathione S-Transferase into Nanowires. *Nanoscale* **2012**, *4* (19), 5847. https://doi.org/10.1039/c2nr31244a.
(20) Yang, M.; Song, W. J. Diverse Protein Assembly Driven by Metal and Chelating Amino Acids with Selectivity and Tunability. *Nat. Commun.* **2019**, *10* (1). https://doi.org/10.1038/s41467-019-13491-w.
(21) Matthaei, J. F.; DiMaio, F.; Richards, J. J.; Pozzo, L. D.; Baker, D.; Baneyx, F. Designing Two-Dimensional Protein Arrays through Fusion of Multimers and Interface Mutations. *Nano Lett.* **2015**, *15* (8), 5235–5239. https://doi.org/10.1021/acs.nanolett.5b01499.
(22) Lo, V.; Ren, Q.; Pham, C.; Morris, V.; Kwan, A.; Sunde, M. Fungal Hydrophobin Proteins Produce Self-Assembling Protein Films with Diverse Structure and Chemical Stability. *Nanomaterials* **2014**, *4* (3), 827–843. https://doi.org/10.3390/nano4030827.
(23) Zhou, K.; Zang, J.; Chen, H.; Wang, W.; Wang, H.; Zhao, G. On-Axis Alignment of Protein Nanocage Assemblies from 2D to 3D through the Aromatic Stacking Interactions of Amino Acid Residues. *ACS Nano* **2018**, *12* (11), 11323–11332. https://doi.org/10.1021/acsnano.8b06091.
(24) Zheng, B.; Zhou, K.; Zhang, T.; Lv, C.; Zhao, G. Designed Two- and Three-Dimensional Protein Nanocage Networks Driven by Hydrophobic Interactions Contributed by Amyloidogenic Motifs. *Nano Lett.* **2019**, *19* (6), 4023–4028. https://doi.org/10.1021/acs.nanolett.9b01365.
(25) Sakai, F.; Yang, G.; Weiss, M. S.; Liu, Y.; Chen, G.; Jiang, M. Protein Crystalline Frameworks with Controllable Interpenetration Directed by Dual Supramolecular Interactions. *Nat. Commun.* **2014**, *5* (1). https://doi.org/10.1038/ncomms5634.
(26) Yang, G.; Ding, H.; Kochovski, Z.; Hu, R.; Lu, Y.; Ma, Y.; Chen, G.; Jiang, M. Highly Ordered Self-Assembly of Native Proteins into 1D, 2D, and 3D Structures Modulated by the Tether Length of Assembly-Inducing Ligands. *Angew. Chem. Int. Ed.* **2017**, *56* (36), 10691–10695. https://doi.org/10.1002/anie.201703052.
(27) Liu, R.; Kochovski, Z.; Li, L.; Yin, Y.; Yang, J.; Yang, G.; Tao, G.; Xu, A.; Zhang, E.; Ding, H.; Lu, Y.; Chen, G.; Jiang, M. Fabrication of Pascal-triangle Lattice of Proteins by Inducing Ligand Strategy. *Angew. Chem. Int. Ed.* **2020**, *59* (24), 9617–9623. https://doi.org/10.1002/anie.202000771.
(28) Sinclair, J. C.; Davies, K. M.; Vénien-Bryan, C.; Noble, M. E. M. Generation of Protein Lattices by Fusing Proteins with Matching Rotational Symmetry. *Nat. Nanotechnol.* **2011**, *6* (9), 558–562. https://doi.org/10.1038/nnano.2011.122.
(29) Zhao, L.; Zou, H.; Zhang, H.; Sun, H.; Wang, T.; Pan, T.; Li, X.; Bai, Y.; Qiao, S.; Luo, Q.; Xu, J.; Hou, C.; Liu, J. Enzyme-Triggered Defined Protein Nanoarrays: Efficient Light-Harvesting Systems to Mimic Chloroplasts. *ACS Nano* **2017**, *11* (1), 938–945. https://doi.org/10.1021/acsnano.6b07527.
(30) Gonen, S.; DiMaio, F.; Gonen, T.; Baker, D. Design of Ordered Two-Dimensional Arrays Mediated by Noncovalent Protein-Protein Interfaces. *Science* **2015**, *348* (6241), 1365–1368. https://doi.org/10.1126/science.aaa9897.

(31) Chen, Z.; Johnson, M. C.; Chen, J.; Bick, M. J.; Boyken, S. E.; Lin, B.; De Yoreo, J. J.; Kollman, J. M.; Baker, D.; DiMaio, F. Self-Assembling 2D Arrays with *de Novo* Protein Building Blocks. *J. Am. Chem. Soc.* **2019**, *141* (22), 8891–8895. https://doi.org/10.1021/jacs.9b01978.
(32) Pyles, H.; Zhang, S.; De Yoreo, J. J.; Baker, D. Controlling Protein Assembly on Inorganic Crystals through Designed Protein Interfaces. *Nature* **2019**, *571* (7764), 251–256. https://doi.org/10.1038/s41586-019-1361-6.
(33) Sayou, C.; Nanao, M. H.; Jamin, M.; Posé, D.; Thévenon, E.; Grégoire, L.; Tichtinsky, G.; Denay, G.; Ott, F.; Peirats Llobet, M.; Schmid, M.; Dumas, R.; Parcy, F. A SAM Oligomerization Domain Shapes the Genomic Binding Landscape of the LEAFY Transcription Factor. *Nat. Commun.* **2016**, *7*, 11222. https://doi.org/10.1038/ncomms11222.
(34) Denay, G.; Chahtane, H.; Tichtinsky, G.; Parcy, F. A Flower Is Born: An Update on Arabidopsis Floral Meristem Formation. *Curr. Opin. Plant Biol.* **2017**, *35*, 15–22. https://doi.org/10.1016/j.pbi.2016.09.003.
(35) Chiari, L.; Carpentier, P.; kieffer-jaquinod, S.; Gogny, A.; Perard, J.; Ravanel, S.; Cobessi, D.; Menage, S.; Dumas, R.; Hamelin, O. LEAFY Protein Crystals with a Honeycomb Structure as Platform for Selective Preparation of Outstanding Stable Bio-Hybrid Materials. *Nanoscale* **2021**. https://doi.org/10.1039/D1NR00268F.
(36) Yang, J.; Zhang, Y. I-TASSER Server: New Development for Protein Structure and Function Predictions. 8.
(37) Nagpal, U.; Müller, M.; Nealey, P. F.; de Pablo, J. J. Free Energy of Defects in Ordered Assemblies of Block Copolymer Domains. *ACS Macro Lett.* **2012**, *1* (3), 418–422. https://doi.org/10.1021/mz200245s.
(38) Sreenivasan, S. V.; Choi, J.; Schumaker, P.; Xu, F. Status of UV Imprint Lithography for Nanoscale Manufacturing. *Compr. Nanosci. Technol.* **2011**, *4*, 83–116. https://doi.org/10.1016/B978-0-12-374396-1.00123-9.
(39) Tan, Y. N.; Lee, J. Y.; Wang, D. I. C. Uncovering the Design Rules for Peptide Synthesis of Metal Nanoparticles. *J. Am. Chem. Soc.* **2010**, *132* (16), 5677–5686. https://doi.org/10.1021/ja907454f.
(40) Taylor, M. T.; Nelson, J. E.; Suero, M. G.; Gaunt, M. J. A Protein Functionalization Platform Based on Selective Reactions at Methionine Residues. *Nature* **2018**, *562* (7728), 563–568. https://doi.org/10.1038/s41586-018-0608-y.
(41) Gunnoo, S. B.; Madder, A. Chemical Protein Modification through Cysteine. *ChemBioChem* **2016**, *17* (7), 529–553. https://doi.org/10.1002/cbic.201500667.
(42) Jung, W.-B.; Jang, S.; Cho, S.-Y.; Jeon, H.-J.; Jung, H.-T. Recent Progress in Simple and Cost-Effective Top-Down Lithography for ≈10 Nm Scale Nanopatterns: From Edge Lithography to Secondary Sputtering Lithography. *Adv. Mater.* **2020**, 1907101. https://doi.org/10.1002/adma.201907101.
(43) Hasan, R. Md. M.; Luo, X. Promising Lithography Techniques for Next-Generation Logic Devices. *Nanomanufacturing Metrol.* **2018**, *1* (2), 67–81. https://doi.org/10.1007/s41871-018-0016-9.
(44) Liddle, J. A.; Gallatin, G. M. Nanomanufacturing: A Perspective. *ACS Nano* **2016**, *10* (3), 2995–3014. https://doi.org/10.1021/acsnano.5b03299.
(45) Bates, C. M.; Maher, M. J.; Janes, D. W.; Ellison, C. J.; Willson, C. G. Block Copolymer Lithography. *Macromolecules* **2014**, *47* (1), 2–12. https://doi.org/10.1021/ma401762n.
(46) Park, S.; Lee, D. H.; Xu, J.; Kim, B.; Hong, S. W.; Jeong, U.; Xu, T.; Russell, T. P. Macroscopic 10-Terabit-per-Square-Inch Arrays from Block Copolymers with Lateral Order. *Science* **2009**, *323* (5917), 1030–1033. https://doi.org/10.1126/science.1168108.
(47) Li, Y.; Xu, Y.; Cao, S.; Zhao, Y.; Qu, T.; Iyoda, T.; Chen, A. Nanoporous Films with Sub-10 Nm in Pore Size from Acid-Cleavable Block Copolymers. *Macromol. Rapid Commun.* **2017**, *38* (5), 1600662. https://doi.org/10.1002/marc.201600662.

(48) Kapadia, R.; Fan, Z.; Takei, K.; Javey, A. Nanopillar Photovoltaics: Materials, Processes, and Devices. *Nano Energy* **2012**, *1* (1), 132–144. https://doi.org/10.1016/j.nanoen.2011.11.002.
(49) Saadi, S.; Nazari, B. Recent Developments and Applications of Nanocomposites in Solar Cells: A Review. *J. Compos. Compd.* **2019**, *1* (1), 34–38. https://doi.org/10.29252/jcc.1.1.7.
(50) Zhou, D.; Pennec, Y.; Djafari-Rouhani, B.; Cristini-Robbe, O.; Xu, T.; Lambert, Y.; Deblock, Y.; Faucher, M.; Stiévenard, D. Optimization of the Optical Properties of Nanostructured Silicon Surfaces for Solar Cell Applications. *J. Appl. Phys.* **2014**, *115* (13), 134304. https://doi.org/10.1063/1.4870236.
(51) Oh, Y.-J.; Kang, M.; Park, M.; Jeong, K.-H. Engineering Hot Spots on Plasmonic Nanopillar Arrays for SERS: A Review. *BioChip J.* **2016**, *10* (4), 297–309. https://doi.org/10.1007/s13206-016-0406-2.
(52) Lee, K.-L.; Hung, C.-Y.; Pan, M.-Y.; Wu, T.-Y.; Yang, S.-Y.; Wei, P.-K. Dual Sensing Arrays for Surface Plasmon Resonance (SPR) and Surface-Enhanced Raman Scattering (SERS) Based on Nanowire/Nanorod Hybrid Nanostructures. *Adv. Mater. Interfaces* **2018**, *5* (21), 1801064. https://doi.org/10.1002/admi.201801064.
(53) Wang, Y.; Becker, M.; Wang, L.; Liu, J.; Scholz, R.; Peng, J.; Gösele, U.; Christiansen, S.; Kim, D. H.; Steinhart, M. Nanostructured Gold Films for SERS by Block Copolymer-Templated Galvanic Displacement Reactions. *Nano Lett.* **2009**, *9* (6), 2384–2389. https://doi.org/10.1021/nl900939y.

For Table of Contents Only